Chemical Science

ROYAL SOCIETY OF CHEMISTRY

EDGE ARTICLE

View Article Online
View Journal | View Issue

Cite this: *Chem. Sci.*, 2021, **12**, 1062

All publication charges for this article have been paid for by the Royal Society of Chemistry

Received 1st October 2020
Accepted 11th November 2020

DOI: 10.1039/d0sc05427e

rsc.li/chemical-science

Mitigation of Jahn–Teller distortion and Na^+/vacancy ordering in a distorted manganese oxide cathode material by Li substitution†

Yanchen Liu, Chenchen Wang, Shuo Zhao, Lin Zhang, Kai Zhang, Fujun Li* and Jun Chen

Layered manganese-based oxides are promising candidates as cathode materials for sodium-ion batteries (SIBs) due to their low cost and high specific capacity. However, the Jahn–Teller distortion from high-spin Mn^{3+} induces detrimental lattice strain and severe structural degradation during sodiation and desodiation. Herein, lithium is introduced to partially substitute manganese ions to form distorted P′2-$Na_{0.67}Li_{0.05}Mn_{0.95}O_2$, which leads to restrained anisotropic change of Mn–O bond lengths and reinforced bond strength in the [MnO_6] octahedra by mitigation of Jahn–Teller distortion and contraction of MnO_2 layers. This ensures the structural stability during charge and discharge of P′2-$Na_{0.67}Li_{0.05}Mn_{0.95}O_2$ and Na^+/vacancy disordering for facile Na^+ diffusion in the Na layers with a low activation energy barrier of ~0.53 eV. It exhibits a high specific capacity of 192.2 mA h g^{-1}, good cycling stability (90.3% capacity retention after 100 cycles) and superior rate capability (118.5 mA h g^{-1} at 1.0 A g^{-1}), as well as smooth charge/discharge profiles. This strategy is effective to tune the crystal structure of layered oxide cathodes for SIBs with high performance.

Introduction

Sodium-ion batteries (SIBs) have attracted extensive attention for large-scale electric energy storage due to the abundance and low cost of sodium resources.[1–3] However, low energy density and insufficient cycling life limit the practical application of SIBs because of the large radius and heavy mass of Na^+.[4,5] Cathode materials play a crucial role in the overall performance and cost of SIBs. Cathode materials with high capacity, long cycling stability and fast Na^+ diffusion are of great significance.[6,7] Among various cathode materials, layered transition metal oxides Na_xTMO_2 (TM = Mn, Co, Ni, Fe, *etc.*) exhibit high Na^+ storage capacities.[8–10] Layered Na_xTMO_2 can be mainly classified into P2 and O3 phases, based on the atomic environment of Na (prismatic or octahedral) and the oxygen layer stacking patterns along the *c*-axis (ABBA or ABCABC).[11,12] P2-Type oxides have more open frameworks and spacious prismatic paths within TMO_2 slabs for direct Na^+ diffusion, which favor rate and cycling capability.[13,14]

P2-Na_xMnO_2 with a hexagonal structure has tremendous potential as a cathode material for SIBs because of the elemental abundance, eco-friendly nature and considerable specific capacity. Particularly, the distorted P′2-$Na_{0.67}MnO_2$ with an orthorhombic structure caused by the Jahn–Teller (J–T) effect exhibits higher capacity than the undistorted P2-$Na_{0.67}MnO_2$.[15–20] However, the J–T distortion, derived from high spin Mn^{3+} (t_{2g}^3–e_g^1), causes an abnormal bond length change of O–Mn–O in [MnO_6] octahedra, large lattice strain and anisotropic volume change during the charge and discharge processes, resulting in Na^+/vacancy ordering and rapid degradation of structural and electrochemical properties of P2/P′2-type $Na_{0.67}MnO_2$.[15,21–23] Due to the lattice distortion in P′2-$Na_{0.67}MnO_2$, a high specific capacity of ~200 mA h g^{-1} can be obtained at the initial cycles, but followed by rapid capacity decay because of the drastic J–T effect during Na^+ extraction/insertion. In order to enhance the structural stability of Mn-based layered oxides, electrochemically inactive ion substitution, such as Mg^{2+}, Al^{3+}, and Zn^{2+}, *etc.*, has been attempted to suppress the J–T effect *via* modulating the electron and bond structure of [MnO_6].[24–27] When doped with Ti, P′2-$Na_{0.67}[(Mn_{0.78}Fe_{0.22})_{0.9}Ti_{0.1}]O_2$ delivers a capacity of ~180 mA h g^{-1} and exhibits reversible Na^+ extraction and insertion for 200 cycles with a retention of 86%.[19] With the introduction of Al into P2-$Na_{0.67}Al_xMn_{1-x}O_2$, the complex phases of P′2 + P2 are electrochemically converted to the undistorted P2, leading to better capacity retentions. The sample doped with 10 mol% Al yields a specific capacity of 175 mA h g^{-1} and long cycling stability exceeding 200 cycles with 85% capacity retention.[26] Achieving the high performance of P′2-$Na_{0.67}MnO_2$, which is limited by

Key Laboratory of Advanced Energy Materials Chemistry (Ministry of Education), Renewable Energy Conversion and Storage Center (RECAST), College of Chemistry, Nankai University, Tianjin 300071, P. R. China. E-mail: fujunli@nankai.edu.cn

† Electronic supplementary information (ESI) available. See DOI: 10.1039/d0sc05427e

the Na^+/vacancy ordering and drastic J–T effect, is still a great challenge for SIBs.

Herein, partial substitution of Li for Mn to form P′2-$Na_{0.67}Li_{0.05}Mn_{0.95}O_2$ is reported. It results in mitigation of J–T distortion and contraction of MnO_2 layers, and then restrains the anisotropic Mn–O bond lengths and reinforces the bond strength in the [MnO_6] octahedra. These strengthened crystal structures and Na^+/vacancy disordering ensure facile Na^+ diffusion. The as-synthesized P′2-$Na_{0.67}Li_{0.05}Mn_{0.95}O_2$ exhibits a high specific capacity of 192.2 mA h g^{-1} within 1.8–4.3 V, good cycling stability and rate capability. This investigation provides insights into the modulation of the chemical environment of redox centers in advanced cathodes for SIBs.

Results and discussion

Structure features

A group of Li-substituted P′2-$Na_{0.67}Li_xMn_{1-x}O_2$ ($x = 0$, 0.03, 0.05 and 0.08) layered oxides were synthesized *via* a facile solid-state reaction at 1000 °C followed by a quenching process. The X-ray diffraction (XRD) patterns and Rietveld refinement of the as-synthesized compounds are presented in Fig. 1a, b, S1 and Tables S1–S4.† All the diffraction peaks of $Na_{0.67}Li_xMn_{1-x}O_2$ can be indexed to an orthorhombic structure with a space group of *Cmcm*.[16] The J–T distortion in the orthorhombic lattice is accompanied by the elongation along the *b* axis and shrinkage along the *a* axis, and the degree of distortion (δ) is determined by using the equation of $b_{ortho}/a_{ortho} = (1+\delta)\sqrt{3}$. The evolution of lattice parameters, Na interlayer spacing ($d_{(Na-O-Na)}$) and δ with the increase of Li content in P′2-$Na_{0.67}Li_xMn_{1-x}O_2$ is depicted in Fig. S2,† which reveals that *a* and $d_{(Na-O-Na)}$ increase with decreasing *b*. Note that P′2-$Na_{0.67}Li_{0.03}Mn_{0.97}O_2$ and P′2-$Na_{0.67}Li_{0.05}Mn_{0.95}O_2$ exhibit similarly decreased degrees of distortion of 6.80% and 6.73% in comparison with 7.68% in P′2-$Na_{0.67}MnO_2$, while P′2-$Na_{0.67}Li_{0.05}Mn_{0.95}O_2$ shows the largest $d_{(Na-O-Na)}$. Though more Li content in P′2-$Na_{0.67}Li_{0.08}Mn_{0.92}O_2$ can lead to smaller δ, the $d_{(Na-O-Na)}$ no longer increases, and redox-active Mn decreases. In the optimal P′2-$Na_{0.67}Li_{0.05}Mn_{0.95}O_2$, obvious shrinkage of bond lengths of Mn–O ($d_{(Mn-O)}$) along the axial O–Mn–O direction and contraction of MnO_2 layers are observed in Fig. S3 and Table S5.† This results in the alleviated anisotropic change of Mn–O bond lengths in the octahedra of [MnO_6] and mitigation of J–T distortion. The elemental composition of P′2-$Na_{0.67}Li_{0.05}Mn_{0.95}O_2$ was determined using an inductively coupled plasma-optical emission spectrometer (ICP-OES), and the result in Table S6† is close to the expected stoichiometry. The robust and shortened Mn–O bond in P′2-$Na_{0.67}Li_{0.05}Mn_{0.95}O_2$ associated with contraction of MnO_2 layers ensures a stable structure, and the enlarged Na interlayer space favors Na^+ diffusion.[13]

To confirm the local environments of Li^+, ^{7}Li solid-state nuclear magnetic resonance (ss-NMR) spectroscopy was carried out for P′2-$Na_{0.67}Li_{0.05}Mn_{0.95}O_2$. As shown in Fig. 1c, the chemical shift values of 1401 ppm and 1318 ppm indicate that Li^+ occupies the octahedral Mn sites in the TMO_2 layer, which is consistent with the chemical shifts of two kinds of Li^+ sites in Li_2MnO_3, namely, in the [MnO_2] and Li layers.[14,28] This can be interpreted as the comparable ionic radii of Li^+ (0.76 Å) and Mn^{3+} (0.65 Å). The X-ray photoelectron spectroscopy (XPS) spectrum of Mn 2p in Fig. 1d shows the electronic structure of Mn in P′2-$Na_{0.67}MnO_2$ and P′2-$Na_{0.67}Li_{0.05}Mn_{0.95}O_2$. Mn 2p in P′2-$Na_{0.67}Li_{0.05}Mn_{0.95}O_2$ shows a higher binding energy, owing to the partial Mn^{3+} oxidation to the J–T inactive Mn^{4+} (t_{2g}^3–e_g^0) *via* Li^+ substitution. The replacement of Mn^{3+} with Li^+ in the octahedral sites increases the average valence of Mn and mitigates the J–T distortion with robust Mn–O bonds, which facilitates the structural stability of P′2-$Na_{0.67}Li_{0.05}Mn_{0.95}O_2$.

The elemental distributions of P′2-$Na_{0.67}Li_{0.05}Mn_{0.95}O_2$ at different depths are recorded by dynamic secondary ion mass spectroscopy (SIMS), as shown in Fig. 1e and S4.† The intensity variation of Na, Li, Mn and O with sputtering time shows the elemental distribution changes at different sputtering depths.[29] The intensity of Na and Li increases rapidly in the initial 50 s, which can be attributed to the minor deposition of impurities during preparation and storage, such as Na_2CO_3 and Li_2CO_3 on the surface. Starting from ~300 s, the concentration of Li and Mn remains steady, showing a homogeneous distribution throughout the bulk. The particle size of P′2-$Na_{0.67}MnO_2$ and P′2-$Na_{0.67}Li_{0.05}Mn_{0.95}O_2$ ranges from 2.0 to 5.0 μm, as shown in the scanning electron microscopy (SEM) images in Fig. S5.† The selected-area electron diffraction (SAED) along the [001] zone of $Na_{0.67}Li_{0.05}Mn_{0.95}O_2$ is presented in Fig. 1f, implying a typical P′2 phase. The crystal lattice spacing in the high-resolution transmission electron microscopy (HRTEM) image of Fig. 1f is 0.56 nm, consistent with the (002) planes of P′2-$Na_{0.67}Li_{0.05}Mn_{0.95}O_2$ and the XRD refinement in Fig. S6.†

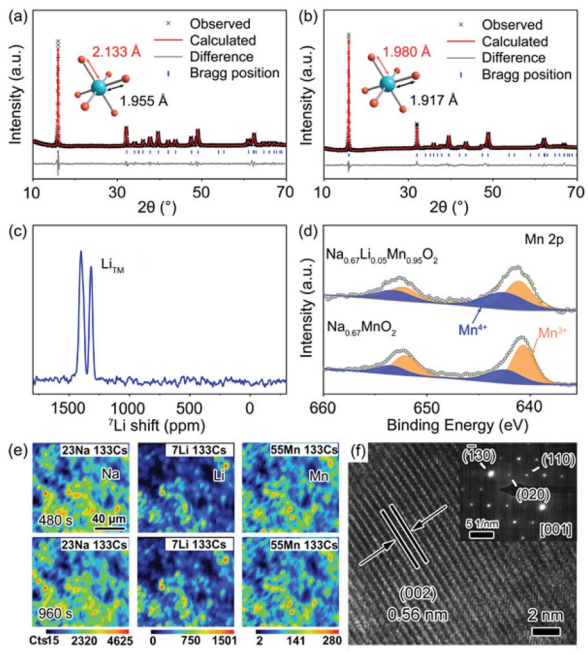

Fig. 1 Rietveld refinement of powder XRD patterns for (a) P′2-$Na_{0.67}MnO_2$ and (b) P′2-$Na_{0.67}Li_{0.05}Mn_{0.95}O_2$. (c) ^{7}Li ss-NMR of P′2-$Na_{0.67}Li_{0.05}Mn_{0.95}O_2$. (d) XPS spectra of the Mn 2p region of $Na_{0.67}MnO_2$ and P′2-$Na_{0.67}Li_{0.05}Mn_{0.95}O_2$. (e) Elemental SIMS mappings and (f) HRTEM and SAED images of P′2-$Na_{0.67}Li_{0.05}Mn_{0.95}O_2$.

Structural evolution and reaction mechanism

The structural evolution of P′2-$Na_{0.67}MnO_2$ and P′2-$Na_{0.67}Li_{0.05}Mn_{0.95}O_2$ during charge and discharge is monitored by *in situ* XRD in a voltage window of 1.8–4.3 V. As shown in Fig. 2a and b, during the initial charge of P′2-$Na_xLi_{0.05}Mn_{0.95}O_2$, the P′2 phase is maintained with $0.26 < x < 0.79$. The *c* parameter increases along with the (002) and (004) peaks shifting to lower angles due to the repulsive force between the adjacent oxygen layers during Na^+ extraction, and the *ab* plane contracts as the (112) peak shifts to higher angles because of the smaller ion radius of Mn at the valence state of 4+.[19,30] The OP4 phase starts to appear upon extraction of ~0.39 mol Na^+ and remains till full charge, as confirmed by the typical OP4 (004) peak at ~17.5° in Fig. 2 and illustrated in Fig. S7†.[31–33] Notably, at the fully charged states, P′2-$Na_xLi_{0.05}Mn_{0.95}O_2$ exhibits a slight variation of $d_{(Mn-O)}$ from 1.980 Å to 1.928 Å, while P′2-Na_xMnO_2 shows an obvious shrinkage from 2.133 to 1.944 Å, based on the Rietveld refinements in Fig. S8 and Table S7.† The robust Mn–O bond enabled by the mitigated J–T distortion due to Li doping ensures structural stability of [MnO_6] octahedra in P′2-$Na_xLi_{0.05}Mn_{0.95}O_2$ upon Na^+ extraction in the charge process.

In the following discharge of P′2-$Na_xLi_{0.05}Mn_{0.95}O_2$, the OP4 phase reversibly transforms to the P′2 phase, as evidenced by the XRD patterns in Fig. 2b. When ~0.65 mol Na^+ is re-inserted into the structure, a two-phase reaction occurs with the phase transformation of P′2 to P″2 due to the dominant Mn^{3+}.[16] The P″2 phase of Na_xMnO_2 exhibits a larger elongation of Mn–O bonds of 2.305 Å in the axial direction than that of $Na_xLi_{0.05}Mn_{0.95}O_2$ (2.230 Å), based on the Rietveld refinements at the discharged state in Fig. S9 and Table S8.† In the meantime, the change of the bond length of the axial Mn–O from OP4 to P″2 in Na_xMnO_2 is 18.57%, in contrast to 15.66% in $Na_xLi_{0.05}Mn_{0.95}O_2$. The degree of distortion of P″2 decreases from 13.37% in P′2-$Na_{0.67}MnO_2$ to 9.30% in P′2-$Na_{0.67}Li_{0.05}Mn_{0.95}O_2$. Particularly, the volume change is merely 1.30% for $Na_xLi_{0.05}Mn_{0.95}O_2$, as compared to 2.61% for P′2-$Na_{0.67}MnO_2$, indicating the alleviated J–T effect.

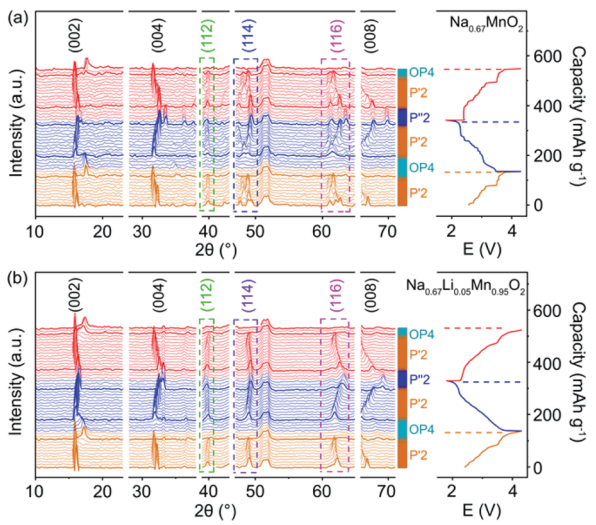

Fig. 2 *In situ* XRD patterns collected in the first cycle and second charge of (a) P′2-$Na_{0.67}MnO_2$ and (b) P′2-$Na_{0.67}Li_{0.05}Mn_{0.95}O_2$.

The P′2 phase of $Na_xLi_{0.05}Mn_{0.95}O_2$ fully recovers from its P″2 phase during the second charge. The reversible phase transitions of P′2-$Na_xLi_{0.05}Mn_{0.95}O_2$ in the charge and discharge process are also revealed by HRTEM and fast Fourier transform (FFT) images shown in Fig. S10.† Meanwhile, asymmetrical shape changes of (112), (114) and (116) are observed in P′2-Na_xMnO_2 ($0.29 < x < 0.77$), corresponding to the multiple stepwise charge/discharge curves in Fig. 2a. This is derived from several phase transitions related to long-range ordering of both Na^+/vacancy and Mn charge,[15,34] which generally leads to severe polarization and poor rate performance.[13,35] However, only peak position shifts are observed in P′2-$Na_xLi_{0.05}Mn_{0.95}O_2$ ($0.26 < x < 0.79$) without asymmetrical diffraction peaks, indicating that the significantly restrained multistep phase transition is related to Na^+/vacancy disordering and a solid–solution reaction process during charge and discharge.

Ex situ XPS was carried out to investigate the charge compensation in P′2-$Na_{0.67}MnO_2$ and P′2-$Na_{0.67}Li_{0.05}Mn_{0.95}O_2$ at different states. Fig. 3a and b show the Mn 2p spectra of the pristine, discharged and charged P′2-$Na_{0.67}MnO_2$ and P′2-$Na_{0.67}Li_{0.05}Mn_{0.95}O_2$, respectively. The two major peaks are deconvoluted into four peaks of Mn $2p_{3/2}$ and Mn $2p_{1/2}$. The two peaks located at 641.7 and 653.2 eV are assigned to Mn^{3+} of the pristine P′2-$Na_{0.67}Li_{0.05}Mn_{0.95}O_2$, while the other two peaks at 643.1 and 654.6 eV correspond to Mn^{4+}. An additional peak at 646.6 eV can be identified as the signal from some Mn ions at higher oxidation state in a fluorine environment.[36] The fluorine mainly comes from additives of fluoroethylene carbonate (FEC) and poly(vinyl difluoride) (PVDF), which are added during the preparation of electrodes. Mn^{3+} is oxidized to Mn^{4+} in the charging process, and a reverse process occurs during discharge, indicating that the Mn^{3+}/Mn^{4+} redox is responsible for the charge compensation (0.72 e^- transfer). As for P′2-$Na_{0.67}MnO_2$, 0.83 e^- transfer occurs during charge/discharge. Hence, the redox couple of Mn^{3+}/Mn^{4+} in both of P′2-$Na_{0.67}MnO_2$ and P′2-$Na_{0.67}Li_{0.05}Mn_{0.95}O_2$ is responsible for the charge and discharge.

Crystal structure and Na^+ kinetics

Theoretical calculations based on density functional theory (DFT) and crystal orbital Hamilton population (COHP) analyses

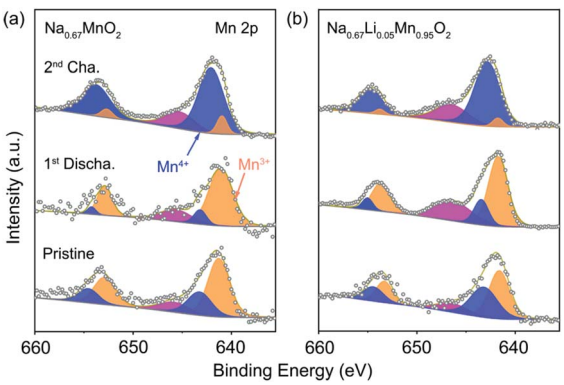

Fig. 3 XPS spectra of Mn 2p collected on the pristine, first discharged and second charged electrode of (a) P′2-$Na_{0.67}MnO_2$ and (b) P′2-$Na_{0.67}Li_{0.05}Mn_{0.95}O_2$.

were performed to explore the bonding situations and structural change with Li^+ doped in P′2-type oxides.[37–39] The structures of P′2-$Na_{0.67}MnO_2$ and P′2-$Na_{0.67}Li_{0.05}Mn_{0.95}O_2$ were optimized based on the Rietveld refinement of XRD data. The geometrical optimization of P′2-$Na_{0.67}MnO_2$ was performed within a $3 \times 1 \times 1$ supercell, which consists of 12 Mn, 8 Na and 24 O atoms. As for P′2-$Na_{0.67}Li_{0.05}Mn_{0.95}O_2$, the structure was obtained *via* replacing one of the Mn atoms by a Li atom in the optimized P′2-$Na_{0.67}MnO_2$. Both of the optimized P′2-$Na_{0.67}MnO_2$ and P′2-$Na_{0.67}Li_{0.05}Mn_{0.95}O_2$ are shown in Fig. 4a and b. The COHP method is efficient to provide the chemical bonding information by indicating "bond-weighted" density of states between the interacting neighbor atoms.[40] Positive and negative values of –COHP suggest the bonding and antibonding interactions, and zero of –COHP indicates a nonbonding interaction. The integrated –COHP shows a bonding interaction between O 2p and Mn 3d, and the intensity of bonding interaction of adjacent Mn–O is strengthened obviously by Li substitution, as depicted in Fig. 4c and d. The stronger Mn–O bonds in [MnO_6] are contributed by the increased hybridization of the O 2p and Mn 3d orbitals, owing to the weak overlap between Li 2s and O 2p orbitals. As shown in Table S9,† the orbital overlap of $Mn_{(11)}$–O in P′2-$Na_{0.67}Li_{0.05}Mn_{0.95}O_2$ increases by 22.67%. The enhanced [MnO_6] slabs result in a robust and stable skeleton to suppress the inferior J–T distortion. Based on the calculated density of states (DOS) of P′2-$Na_{0.67}MnO_2$ and P′2-$Na_{0.67}Li_{0.05}Mn_{0.95}O_2$ in Fig. S11,† the number of electrons in Mn e_g orbitals decreases obviously for Li^+-doped material, suggesting that some Mn^{3+} ions are oxidized and the J–T inactive Mn^{4+} centers increase.

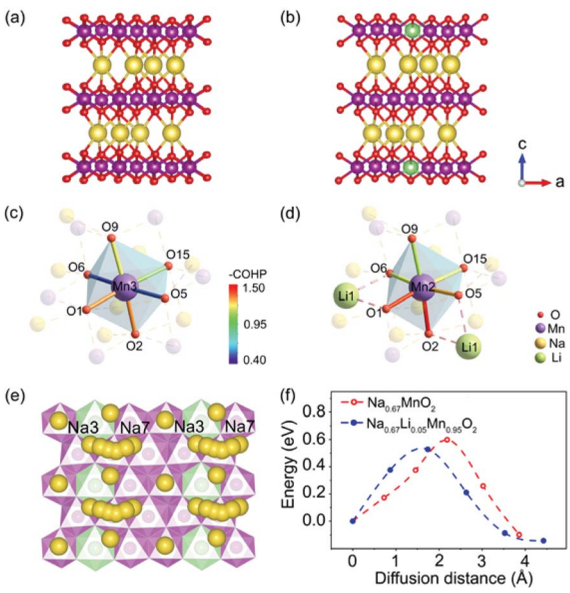

Fig. 4 Optimized structure of (a) P′2-$Na_{0.67}MnO_2$ and (b) P′2-$Na_{0.67}Li_{0.05}Mn_{0.95}O_2$. COHP analysis of the transition metal octahedral sites of (c) P′2-$Na_{0.67}MnO_2$ and (d) P′2-$Na_{0.67}Li_{0.05}Mn_{0.95}O_2$. (e) Na3–Na7 diffusion pathway in P′2-$Na_{0.67}Li_{0.05}Mn_{0.95}O_2$. (f) activation energy barrier for Na^+ diffusion in P′2-$Na_{0.67}MnO_2$ and P′2-$Na_{0.67}Li_{0.05}Mn_{0.95}O_2$.

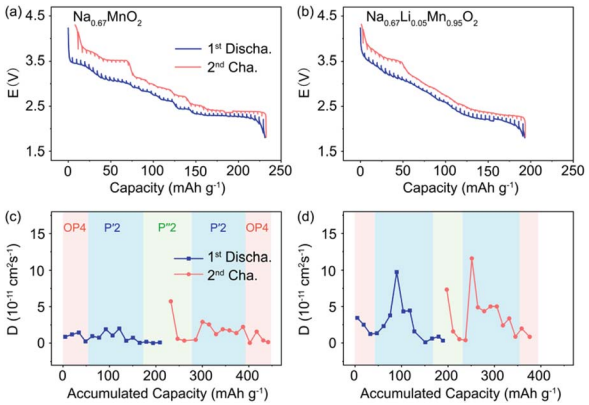

Fig. 5 GITT profiles of (a) P′2-$Na_{0.67}MnO_2$ and (b) P′2-$Na_{0.67}Li_{0.05}Mn_{0.95}O_2$ in a charge and discharge cycle. Na^+ diffusion coefficients of (c) P′2-$Na_{0.67}MnO_2$ and (d) P′2-$Na_{0.67}Li_{0.05}Mn_{0.95}O_2$ calculated from GITT measurements.

The activation energy barrier of Na^+ in P′2-$Na_{0.67}MnO_2$ and P′2-$Na_{0.67}Li_{0.05}Mn_{0.95}O_2$ was calculated using the climbing image nudged elastic band (CINEB) method. As shown in Fig. 4e and f, the activation energy barrier is ~0.53 eV in P′2-$Na_{0.67}Li_{0.05}Mn_{0.95}O_2$ along the Na3–Na7 pathway in the *ab* plane, which is 0.07 eV lower than that in P′2-$Na_{0.67}MnO_2$. Furthermore, the Na^+ diffusion coefficients were investigated using the galvanostatic intermittent titration technique (GITT). In contrast, P′2-$Na_{0.67}Li_{0.05}Mn_{0.95}O_2$ displays smaller voltage hysteresis and high coulombic efficiency in the GITT curves (Fig. 5a and b). The calculated Na^+ diffusion coefficients of P′2-$Na_{0.67}Li_{0.05}Mn_{0.95}O_2$ range from 2.0×10^{-11} to 10^{-10} cm^2 s^{-1} within the scope of the solid–solution reaction, which are an order of magnitude higher than those of P′2-$Na_{0.67}MnO_2$ (Fig. 5c and d). The results are in good agreement with the calculation of activation barriers in Fig. 4f and the smooth charge and discharge curves in Fig. 2. Lower polarization and activation energy barrier, as well as increased Na^+ diffusion kinetics, are realized by virtue of the expanded Na^+ layer spacing and suppressed Na^+/vacancy ordering by Li doping.

Electrochemical performance

The electrochemical performance of P′2-$Na_{0.67}MnO_2$ and P′2-$Na_{0.67}Li_{0.05}Mn_{0.95}O_2$ was examined in coin cells with Na as the negative electrode. Fig. 6a and b exhibit the galvanostatic charge/discharge curves of P′2-$Na_{0.67}MnO_2$ and P′2-$Na_{0.67}Li_{0.05}Mn_{0.95}O_2$ in the initial three cycles at 20 mA g^{-1} within 1.8–4.3 V. P′2-$Na_{0.67}MnO_2$ delivers a high initial discharge capacity of 217.6 mA h g^{-1} (0.83 Na^+) but severe capacity and voltage fading during the first three cycles. The multiple stepwise curves observed in P′2-$Na_{0.67}MnO_2$ are assigned to the phase transitions and Na^+/vacancy ordering. In contrast, P′2-$Na_{0.67}Li_{0.05}Mn_{0.95}O_2$ displays smooth and highly overlapped charge/discharge profiles with a reversible capacity of 192.2 mA h g^{-1} (0.72 Na^+), which are attributed to the solid–solution reaction process between 2.1 and 3.6 V. The specific capacity decreases with the increased content of Li, because the inactive Li^+ dopant

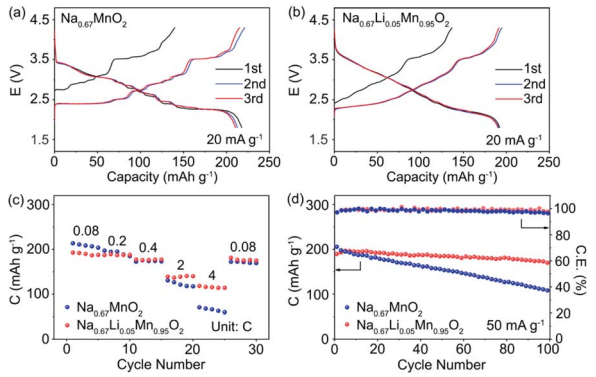

Fig. 6 Charge and discharge profiles of (a) P′2-$Na_{0.67}MnO_2$ and (b) P′2-$Na_{0.67}Li_{0.05}Mn_{0.95}O_2$ at 20 mA g^{-1}. (c) Rate capability comparison of and P′2-$Na_{0.67}MnO_2$ and P′2-$Na_{0.67}Li_{0.05}Mn_{0.95}O_2$ at different rates. (d) Cycle performance of P′2-$Na_{0.67}MnO_2$ and P′2-$Na_{0.67}Li_{0.05}Mn_{0.95}O_2$ at 50 mA g^{-1}.

does not participate in the electrochemical reaction but can effectively restrain the unfavorable Na^+/vacancy ordering.

The cyclic voltammograms (CV) and dQ/dE curves of P′2-$Na_{0.67}MnO_2$ in Fig. S12 and S13† show two main pairs of peaks at 3.54/3.39 and 2.50/2.19 V and additional multiple redox peaks, which are assigned to the phase transition reaction and Na^+/vacancy ordering.[15] The multiple redox peaks of $Na_{0.67}Li_x$-$Mn_{1-x}O_2$ ($x = 0.03$, 0.05 and 0.08) weaken, and disappear when the Li content increases, further indicating that the Na^+/vacancy ordering can be suppressed by substitution of Mn^{3+} with Li^+. In addition, based on the equation $i = av^b$, capacitive storage of Na^+ in P′2-$Na_{0.67}Li_xMn_{1-x}O_2$ ($x = 0$, 0.05 and 0.08) is demonstrated by quantitative electrochemical kinetics calculation, in which the values of b determining the sodiation and desodiation behaviors are exhibited in Fig. S14.† This indicates that the electrochemical process is partially controlled by capacitive behavior. The capacitive contribution of peak 1 of P′2-$Na_{0.67}$-$Li_{0.05}Mn_{0.95}O_2$ ranges from 44.12% to 72.58% at the various scan rates from 0.1 to 1.0 mV s^{-1}. A larger capacitive contribution can be observed with the increase of Li content. Fig. 6c presents the rate capability of P′2-$Na_{0.67}MnO_2$ and P′2-$Na_{0.67}$-$Li_{0.05}Mn_{0.95}O_2$ at various current densities ranging from 0.08 to 4C. (1C = 250 mA g^{-1}). P′2-$Na_{0.67}Li_{0.05}Mn_{0.95}O_2$ delivers high reversible capacities of 187.3, 177.3, 139.2 and 118.5 mA h g^{-1} at 0.2, 0.4, 2 and 4C, respectively. The superior rate capability of P′2-$Na_{0.67}Li_{0.05}Mn_{0.95}O_2$ is benefited from its expanded spacing of Na^+ layers and solid–solution reaction with fast Na^+ kinetics.

The long-term cycling stability of prepared P′2-$Na_{0.67}MnO_2$ and P′2-$Na_{0.67}Li_{0.05}Mn_{0.95}O_2$ within 1.8–4.3 V at the current of 50 mA g^{-1} is shown in Fig. 6d. P′2-$Na_{0.67}Li_{0.05}Mn_{0.95}O_2$ exhibits good capacity retention of 90.3% after 100 cycles, corresponding to a capacity loss of around 0.097% per cycle. The coulombic efficiency of P′2-$Na_{0.67}Li_{0.05}Mn_{0.95}O_2$ remains above 99%. In contrast, the capacity retention of P′2-$Na_{0.67}MnO_2$ is only 48.0% after 100 cycles. This is attributed to the Li incorporation in P′2-$Na_{0.67}Li_{0.05}Mn_{0.95}O_2$, which can effectively suppress the J–T distortion and Na^+/vacancy ordering and facilitate the structural stability and facile Na^+ transport.

Conclusions

In summary, Li substitution in P′2-$Na_{0.67}MnO_2$ has been demonstrated to be an impactful strategy to suppress the detrimental J–T distortion and Na^+/vacancy ordering to enhance its structural stability. The inactive Li^+ in the TMO_2 layers tends to prevent the anisotropic change of the Mn–O bond and promotes its bond strength, leading to a more stable skeleton and contraction of TMO_2 layers. The J–T distortion of [MnO_6] octahedra in P′2-$Na_{0.67}Li_{0.05}Mn_{0.95}O_2$ is effectively mitigated during phase transitions, and the volume change in P′2–P″2 transition is merely 1.30%, which enable good cycling stability (90.3% capacity retention after 100 cycles at 50 mA g^{-1}). The suppressed Na^+/vacancy ordering with enlarged Na interlayer spacing and low activation energy barrier (~0.53 eV) yields superior rate capability (118.5 mA h g^{-1} at 1.0 A g^{-1}). This investigation sheds light on the design of advanced electrode materials by tuning their chemical environments for high-performance SIBs.

Conflicts of interest

There are no conflicts to declare.

Acknowledgements

Financial support from the National Natural Science Foundation of China (grant no. 21835004, 21822506, and 51761165025), the Tianjin Natural Science Foundation (grant no. 19JCJQJC62400), and the 111 project of B12015 is acknowledged.

Notes and references

1 Q. Wang, S. Mariyappan, J. Vergnet, A. M. Abakumov, G. Rousse, F. Rabuel, M. Chakir and J.-M. Tarascon, *Adv. Energy Mater.*, 2019, **9**, 1901785.
2 C. Zhao, Z. Yao, Q. Wang, H. Li, J. Wang, M. Liu, S. Ganapathy, Y. Lu, J. Cabana, B. Li, X. Bai, A. Aspuru-Guzik, M. Wagemaker, L. Chen and Y.-S. Hu, *J. Am. Chem. Soc.*, 2020, **142**, 5742.
3 C. Wang, D. Du, M. Song, Y. Wang and F. Li, *Adv. Energy Mater.*, 2019, **9**, 1900022.
4 X. Zhang, S. Guo, P. Liu, Q. Li, S. Xu, Y. Liu, K. Jiang, P. He, M. Chen, P. Wang and H. Zhou, *Adv. Energy Mater.*, 2019, **9**, 1900189.
5 C. Wang, L. Wang, F. Li, F. Cheng and J. Chen, *Adv. Mater.*, 2017, **29**, 1702212.
6 K. Jiang, S. Xu, S. Guo, X. Zhang, X. Zhang, Y. Qiao, T. Fang, P. Wang, P. He and H. Zhou, *Nano Energy*, 2018, **52**, 88.
7 B. Cao, Z. Liu, C. Xu, J. Huang, H. Fang and Y. Chen, *J. Power Sources*, 2019, **414**, 233.
8 P.-F. Wang, M. Weng, Y. Xiao, Z. Hu, Q. Li, M. Li, Y.-D. Wang, X. Chen, X. Yang, Y. Wen, Y.-X. Yin, X. Yu, Y. Xiao, J. Zheng, L.-J. Wan, F. Pan and Y.-G. Guo, *Adv. Mater.*, 2019, **31**, 1903483.

9 Y. Xiao, N. M. Abbasi, Y.-F. Zhu, S. Li, S.-J. Tan, W. Ling, L. Peng, T. Yang, L. Wang, X.-D. Guo, Y.-X. Yin, H. Zhang and Y.-G. Guo, *Adv. Funct. Mater.*, 2020, **30**, 2001334.
10 X. Rong, E. Hu, Y. Lu, F. Meng, C. Zhao, X. Wang, Q. Zhang, X. Yu, L. Gu, Y.-S. Hu, H. Li, X. Huang, X.-Q. Yang, C. Delmas and L. Chen, *Joule*, 2019, **3**, 1.
11 L. Mu, X. Feng, R. Kou, Y. Zhang, H. Guo, C. Tian, C.-J. Sun, X.-W. Du, D. Nordlund, H. L. Xin and F. Lin, *Adv. Energy Mater.*, 2018, **8**, 1801975.
12 C. Ma, J. Alvarado, J. Xu, R. J. Clément, M. Kodur, W. Tong, C. P. Grey and Y. S. Meng, *J. Am. Chem. Soc.*, 2017, **139**, 4835.
13 P.-F. Wang, H.-R. Yao, X.-Y. Liu, Y.-X. Yin, J.-N. Zhang, Y. Wen, X. Yu, L. Gu and Y.-G. Guo, *Sci. Adv.*, 2018, **4**, eaar6018.
14 J. Xu, D. H. Lee, R. J. Clément, X. Yu, M. Leskes, A. J. Pell, G. Pintacuda, X.-D. Yang, C. P. Grey and Y. S. Meng, *Chem. Mater.*, 2014, **26**, 1260.
15 S. Kumakura, Y. Tahara, K. Kubota, K. Chihara and S. Komaba, *Angew. Chem., Int. Ed.*, 2016, **55**, 12760.
16 S. Kumakura, Y. Tahara, S. Sato, K. Kubota and S. Komaba, *Chem. Mater.*, 2017, **29**, 8958.
17 R. Stoyanova, D. Carlier, M. Sendova-Vassilev, M. Yoncheva, E. Zhecheva, D. Nihtianova and C. Delmas, *J. Solid State Chem.*, 2010, **183**, 1372.
18 J. U. Choi, C. S. Yoon, Q. Zhang, P. Kaghazchi, Y. H. Jung, K.-S. Lee, D.-C. Ahn, Y.-K. Sun and S.-T. Myung, *J. Mater. Chem. A*, 2019, **7**, 202.
19 Y. J. Park, J. U. Choi, J. H. Jo, C.-H. Jo, J. Kim and S.-T. Myung, *Adv. Funct. Mater.*, 2019, **29**, 1901912.
20 J. U. Choi, Y. J. Park, J. H. Jo, L.-Y. Kuo, P. Kaghazchi and S.-T. Myung, *ACS Appl. Mater. Interfaces*, 2018, **10**, 40978.
21 A. Mullaliu, M. Gaboardi, J. R. Plaisier, S. Passerini and M. Giorgetti, *ACS Appl. Energy Mater.*, 2020, **3**, 5728.
22 X. Li, X. Ma, D. Su, L. Liu, R. Chisnell, S. P. Ong, H. Chen, A. Toumar, J.-C. Idrobo, Y. Lei, J. Bai, F. Wang, J. W. Lynn, Y. S. Lee and G. Ceder, *Nat. Mater.*, 2014, **13**, 586.
23 K. Lei, Z. Zhu, Z. Yin, P. Yan, F. Li and J. Chen, *Chem*, 2019, **5**, 3220.
24 R. J. Clément, J. Billaud, A. R. Armstrong, G. Singh, T. Rojo, P. G. Bruce and C. P. Grey, *Energy Environ. Sci.*, 2016, **9**, 3240.
25 J. Billaud, G. Singh, A. R. Armstrong, E. Gonzalo, V. Roddatis, M. Armand, T. Rojo and P. G. Bruce, *Energy Environ. Sci.*, 2014, **7**, 1387.
26 X. Liu, W. Zuo, B. Zheng, Y. Xiang, K. Zhou, Z. Xiao, P. Shan, J. Shi, Q. Li, G. Zhong, R. Fu and Y. Yang, *Angew. Chem., Int. Ed.*, 2019, **58**, 18086.
27 K. Zhang, D. Kin, Z. Hu, M. Park, G. Noh, Y. Yang, J. Zhang, V. W.-H. Lau, S.-L. Chou, M. Cho, S.-Y. Choi and Y.-M. Kang, *Nat. Commun.*, 2019, **10**, 1.
28 C. P. Grey and N. Dupré, *Chem. Rev.*, 2004, **104**, 4493–4512.
29 Z. Yan, L. Tang, Y. Huang, W. Hua, R. Liu, Q. Gu, S. Indris, S.-L. Chou, Y. Huang, M. Wu and S.-X. Dou, *Angew. Chem., Int. Ed.*, 2019, **131**, 1426.
30 Q.-C. Wang, J.-K. Meng, X.-Y. Yue, Q.-Q. Qiu, Y. Song, X.-J. Wu, Z.-W. Fu, Y.-Y. Xia, Z. Shadike, J. Wu, X.-Q. Yang and Y.-N. Zhou, *J. Am. Chem. Soc.*, 2018, **141**, 840.
31 J.-Y. Hwang, J. Kim, T.-Y. Yu and Y.-K. Sun, *Adv. Energy Mater.*, 2019, **9**, 1803346.
32 N. Yabuuchi, M. Kajiyama, J. Iwatate, H. Nishikawa, S. Hitomi, R. Okuyama, R. Usui, Y. Yamada and S. Komaba, *Nat. Mater.*, 2012, **11**, 512.
33 W. K. Pang, S. Kalluri, V. K. Peterson, N. Sharma, J. Kimpton, B. Johannessen, H. K. Liu, S. X. Dou and Z. Guo, *Chem. Mater.*, 2015, **27**, 3150.
34 Y. Wang, R. Xiao, Y.-S. Hu, M. Avdeev and L. Chen, *Nat. Commun.*, 2015, **6**, 1.
35 S. M. Kang, J.-H. Park, A. Jin, Y. H. Jung, Y. H. Jung, J. Mun and Y.-E. Sung, *ACS Appl. Mater. Interfaces*, 2018, **10**, 3562–3570.
36 W. Li and B. L. Lucht, *J. Power Sources*, 2007, **168**, 258.
37 S. Steinberg and R. Dronskowski, *Crystals*, 2018, **8**, 225.
38 R. Dronskowski and P. E. Bloechl, *J. Phys. Chem.*, 1993, **97**, 8617.
39 S. Maintz, V. L. Deringer, A. L. Tchougréeff and R. Dronskowski, *J. Comput. Chem.*, 2016, **37**, 1030.
40 G. Kresse and J. Hafner, *Phys. Rev. B: Condens. Matter Mater. Phys.*, 1993, **47**, 558–561.